

# Thermal circuit model for silicon quantum-dot array structures

Takeru Utsugi,<sup>1, a)</sup> Nobuhiro Kusuno,<sup>1</sup> Takuma Kuno,<sup>1</sup> Noriyuki Lee,<sup>1</sup> Itaru Yanagi,<sup>1</sup> Toshiyuki Mine,<sup>1</sup> Shinichi Saito,<sup>1</sup> Digh Hisamoto,<sup>1</sup> Ryuta Tsuchiya,<sup>1</sup> and Hiroyuki Mizuno<sup>1</sup>

*Research & Development Group, Hitachi, Ltd., Kokubunji, Tokyo 185-8601, Japan*

(Dated: 20 December 2024)

Temperature rise of qubits due to heating is a critical issue in large-scale quantum computers based on quantum-dot (QD) arrays. This leads to shorter coherence times, induced readout errors, and increased charge noise. Here, we propose a simple thermal circuit model to describe the heating effect on silicon QD array structures. Noting that the QD array is a periodic structure, we represent it as a thermal distributed-element circuit, forming a thermal transmission line. We validate this model by measuring the electron temperature in a QD array device using Coulomb blockade thermometry, finding that the model effectively reproduces experimental results. This simple and scalable model can be used to develop the thermal design of large-scale silicon-based quantum computers.

## I. INTRODUCTION

Silicon quantum-dot (QD) arrays are promising candidates for scalable quantum computing platforms because of their outstanding transistor integration, long coherence time, and high fidelity<sup>1–9</sup>. For realizing a large-scale integration, heating in the QD array is an unavoidable issue. The rise in electron (or hole) temperature due to heating leads to shorter coherence times, induced readout errors, and increased charge noise<sup>2,10</sup>. There are several heat sources (e.g., heat and thermal noise inflows through wires, loss of microwave signals, and driving in charge sensors) that are expected to escalate with the large-scale integration of qubits<sup>11–16</sup>.

Two approaches have been investigated to address the heating problem. One is to develop cryo-electronics, effectively reducing the wiring from room temperature and reducing the heat input from the wiring<sup>17–19</sup>. The other is operating qubits at high temperature using heat-tolerant techniques, such as a Pauli spin blockade readout, which has been demonstrated to operate at temperatures as high as one kelvin<sup>10,20–25</sup>. Meanwhile, we are exploring another approach, namely thermal management through the design of heat inflow paths in QD array structures and the control of heat sources using real-time ambient temperature measurements. To achieve this, the thermal conduction characteristics of the device need to be understood. To accurately measure the thermal characteristics, local heaters and thermometers must be integrated into the QD array.

Coulomb blockade thermometry (CBT) is known to measure temperature in QD structures in cryogenic environments<sup>26–28</sup>. CBT has been used to study the thermal conduction properties of quantum point contacts (QPCs)<sup>29,30</sup> and single-electron transistors (SETs)<sup>31–33</sup> in cryogenic environments. However, the thermal conduction characteristics of QD array structures have yet to be investigated. Recently, thermal analysis towards

silicon quantum computers has been conducted. Heating in cryo-electronic circuits was investigated using two transistors for the local heater and CBT sensor<sup>34</sup>, and thermal transient in QD array structure was obtained by using microwave pulses and reflectometry<sup>35</sup>. Furthermore, the thermal circuit model based on the lumped-element model was developed to analyze the cryogenic CMOS on-chip thermometry, a crucial step for understanding the thermal characteristics in cryo-chips<sup>15</sup>.

In this paper, to clarify the thermal conduction characteristics of QD array structures, we propose a simple thermal circuit model. In Sec. II, we explain our model, where the QD array structure is described by an effective thermal circuit based on the distributed-element model. This results in an analytical expression of the thermal transmission line. In Sec. III, we show the experimental validation of our model, where we measure the electron temperature in a QD array device using CBT. A local heater is implemented by flowing current through the barrier gates of the QD array. This experimental setup mimics the heat generated by the local current flowing through the gate wiring for the qubit addressing<sup>6,13</sup> and by the microwaves applied to the gate wiring for an electric dipole spin resonance<sup>1</sup>. From the distance dependence between the local heater and the SET, we find that this model reproduces the experimental results. In Sec. IV, we discuss the limitations of our model and future work. Our proposed model is simple, intuitive, and scalable and can be used for the thermal management of large-scale quantum computers in silicon.

## II. MODEL

We describe the heating effects in silicon quantum computers separately in three parts: (a) Heating source, (b) heat flow, and (c) qubits. Figure 1 illustrates a conceptual diagram. In silicon quantum computers that are typically implemented in cryogenic environments using dilution refrigerators, there are several heat sources such as radiation within dilution refrigerator, heat and thermal noise inflows through wires, loss of microwave signals,

<sup>a)</sup>takeru.utsugi.qb@hitachi.com

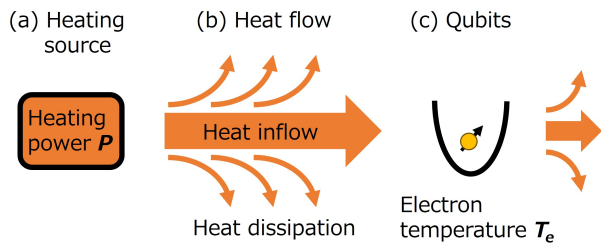


FIG. 1. Conceptual diagram of the heating effects in silicon quantum computers. Heat flow is modeled by describing the electron temperature  $T_e$  of qubits as a function of the heating power  $P$  and various parameters that depend on the device structure.

and local currents in charge sensors<sup>11–16</sup>. These heat sources can be modeled as heating power  $P$ . The heat inflow to the qubits and the heat dissipation to the cooler depend on the device structure, specifically its thermal conductance and capacitance. Our objective is to model the electron temperature of qubits  $T_e$  as a function of  $P$  and various parameters depending on the device structure. By employing this model, we can estimate  $T_e$  from  $P$  to design the heat flow path accordingly.

For constructing the thermal model of the silicon QD array, we note that typical silicon QD array structures are configured with a periodic gate array<sup>3–9</sup>, and this periodicity is essential for modeling their thermal characteristics. In our model, the QD array device is represented as a periodic structure shown in Fig. 2(a). The unit cell comprises a set of a plunger gate (PG), barrier gate (BG), and insulators such as SiO<sub>2</sub>, where the length of the unit cell in  $x$  direction is  $L_{\text{cell}}$ . For simplicity, the silicon channel and the regions outside the gate structure are omitted. Heat flow is considered two-dimensional due to the presence of thick SiO<sub>2</sub> or Si layers at the top and bottom, which have lower thermal conductivity than the gate structures made of metal or polysilicon at cryogenic temperatures. This heat flow is divided into two paths: heat inflow path and dissipation path. The heat inflow path represents the propagation of heat from the source to the qubits along the periodic gate structure, while the dissipation path represents the heat propagation from the heat source to the cooler. Here, the heat flow that does not reach the qubits is dissipated through a medium with high thermal conductivity, such as metallic gates, metallic wires, and metallic structure in a dilution refrigerator.

In our model, the thermal structure of the QD array is simplified as a thermal rod, as shown in Fig. 2(b). We employ a thermal circuit model where thermal characteristics are analogously represented to an electrical circuit. In this model, heating power and temperature are represented by current and voltage, respectively, similar to an electrical circuit model<sup>15</sup>. Thus, periodic structures can be modeled using a thermal distributed-element model, analogous to the transmission line model in electrical circuits. We show the thermal circuit diagram for the ther-

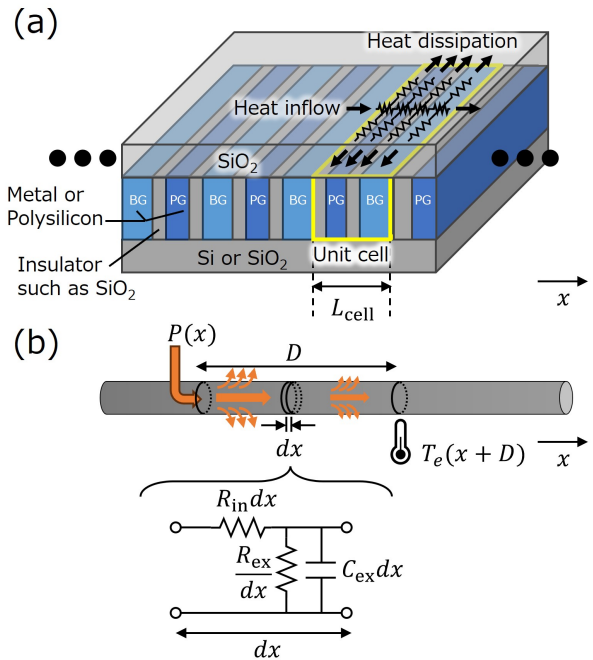


FIG. 2. (a) Model of the silicon QD array structure. The periodic gate structure comprises the plunger gate (PG) and the barrier gate (BG) made of metal or polysilicon. Top and bottom layers are thick Si or SiO<sub>2</sub>. Heat inflow propagates to the  $x$  direction, and heat dissipation propagates to the other directions. (b) Simplified thermal rod model for periodic structure in (a) and the thermal circuit analogous to the transmission line in an electric circuit.

mal rod in Fig. 2(b), where unlike in the case of electronic circuits, inductors are excluded. This thermal circuit can be analyzed using the telegrapher’s equations. In this context,  $R_{\text{in}}$  (heat inflow resistance),  $R_{\text{ex}}$  (heat dissipation resistance), and  $C_{\text{ex}}$  (heat capacitance) are defined as distributed elements, as shown in Fig. 2(b).

Here, we outline the assumptions underlying our model. (i) The first assumption is that the thermal circuit consists of an infinite periodic structure. This assumption is valid for large-scale QD array structures and thermally uniform structures such as those incorporating dummy metals in the gate layer. (ii) The second assumption is that the distributed elements of the thermal circuit,  $R_{\text{in}}$ ,  $R_{\text{ex}}$ , and  $C_{\text{ex}}$ , are temperature dependent and spatially uniform. To account for the temperature dependence of these spatially uniform circuit elements, we consider the device’s net effective temperature, which is the spatially averaged temperature in the area to be analyzed. (iii) The third assumption is that this net effective temperature is proportional to  $T_e$ . This is an assumption that is also applied in Ref.<sup>15</sup>. These assumptions allow us to use a transmission line model based on the distributed-element model. While the distributed circuit elements are spatially uniform, the spatial temperature distribution of the QD array is not uniform and decays exponentially [as derived in following Eq. (4)]. The ap-

proximation error arising from this inconsistency is minimized when the spatial temperature variation is smaller than the net effective temperature.

We then explain the thermal circuit elements  $R_{\text{in}}$ ,  $R_{\text{ex}}$ , and  $C_{\text{ex}}$ , respectively.  $R_{\text{in}}$  is the thermal resistance (per unit length) for heat inflow from the heat source to the temperature measurement point (qubit). This thermal resistance is a series of resistances of a periodic structure, which is composed of the metallic or polysilicon gates and the insulator (we show the order estimation of  $R_{\text{in}}$ , see Appendix C). On the basis of the above discussion, we use  $R_{\text{in}} \propto 1/T_e^{\beta_{\text{in}}}$ , where  $\beta_{\text{in}}$  depends on the thermal conductivity in cryogenic regime and the thickness of the gate and insulator. For example,  $\beta_{\text{in}} \approx 1$  when the gate is dominant and  $\beta_{\text{in}} \approx 2$  when the insulator (amorphous  $\text{SiO}_2$ ) is dominant (see Appendix A).

$R_{\text{ex}}$  is the thermal resistance (inverse of the thermal conductance per unit length) for heat dissipation from the heat source. Heat is dissipated through metallic wires and metallic structures in a dilution refrigerator and is finally collected in the mixing chamber, which acts as a cooler. Therefore,  $R_{\text{ex}}$  depends on the structure of the whole chip and chip's implementation form such as the circuit board mounting the chip, bonding wires, sample packaging, and cables. Most of these materials are metallic. We then use  $R_{\text{ex}} \propto 1/T_e^{\beta_{\text{ex}}}$ , where  $\beta_{\text{ex}} \approx 1$  considering the metallic materials are dominant (see Appendix A).

The heat capacitance  $C_{\text{ex}}$  is crucial for real-time thermal management because it influences the temporal changes in device temperature, which is essential for understanding the dynamic temperature effects on qubits, such as heat-induced frequency shifts<sup>14,16,36</sup>. It is noted that specific heat changes drastically (approximately  $\propto T^3$ ) at cryogenic temperatures, according to the Debye model, as shown in Appendix A.

In analogy to transmission line models in electrical circuits,  $T_e$ , the temperature of the thermal rod at a point that is a distance  $D$  away from the heat source having heating power  $P$ , can be derived as follows. From the telegrapher's equations, we obtain the relations  $T_e(x+D) = T_e(x)e^{-\gamma_{\text{th}}D}$ ,  $P(x+D) = P(x)e^{-\gamma_{\text{th}}D}$ , and  $T_e(x) = Z_{\text{th}}P(x)$ , where the position on the thermal rod  $x$ , thermal characteristic impedance  $Z_{\text{th}}$  and thermal propagation constant  $\gamma_{\text{th}}$  are introduced. From these relations, we can describe

$$T_e(x+D) = Z_{\text{th}}e^{-\gamma_{\text{th}}D}P(x). \quad (1)$$

Since  $x$  is arbitrary, we will denote  $T_e(x+D)$  simply as  $T_e$  and  $P(x)$  as  $P$  from here on.

We then describe  $Z_{\text{th}}$  and  $\gamma_{\text{th}}$  as

$$Z_{\text{th}} = \sqrt{\frac{R_{\text{in}}}{\left(\frac{1}{R_{\text{ex}}} + j\omega C_{\text{ex}}\right)}} \approx \sqrt{R_{\text{in}}R_{\text{ex}}} \approx a^{1+\beta}/T_e^\beta, \quad (2)$$

$$\gamma_{\text{th}} = \sqrt{R_{\text{in}}\left(\frac{1}{R_{\text{ex}}} + j\omega C_{\text{ex}}\right)} \approx \sqrt{\frac{R_{\text{in}}}{R_{\text{ex}}}}, \quad (3)$$

where  $j$  and  $\omega$  are the imaginary unit and angular frequency of thermal behaviors, respectively. The terms  $a$  and  $\beta$  are constant parameters depending on the device, where  $\beta = (\beta_{\text{in}} + \beta_{\text{ex}})/2$ . In the first approximation in Eqs. (2) and (3),  $\omega$  is set to zero to perform the static analysis. The second approximation in Eq. (2) is derived by the relations  $R_{\text{in}} \propto 1/T_e^{\beta_{\text{in}}}$  and  $R_{\text{ex}} \propto 1/T_e^{\beta_{\text{ex}}}$ .

Substituting Eq. (2) into Eq. (1), we obtain

$$T_e \approx ae^{-\frac{\gamma_{\text{th}}}{1+\beta}D}P^{\frac{1}{1+\beta}}. \quad (4)$$

This result indicates that the electron temperature is modeled as a function of heating power  $P$ , the distance  $D$ , and three device-dependent parameters ( $a$ ,  $\gamma_{\text{th}}$ , and  $\beta$ ).

Hereafter, for simplicity, we use  $\beta_{\text{in}} \approx \beta_{\text{ex}} \approx 1$ , i.e.,  $\beta \approx 1$ . This approximation is valid because, in a typical QD array structure, the thickness of the insulator is relatively lower than that of the gate, justifying  $\beta_{\text{in}} \approx 1$ . Similarly,  $\beta_{\text{ex}} \approx 1$  is valid considering that metallic materials dominate the heat dissipation path, as mentioned above. Therefore, we can rewrite Eq. (4) as

$$T_e \approx ae^{-\frac{\gamma_{\text{th}}}{2}D}\sqrt{P}. \quad (5)$$

We note that  $a$  depends on the multiple of the thermal resistances ( $R_{\text{in}} \times R_{\text{ex}}$ ) from Eq. (2). On the other hand,  $\gamma_{\text{th}}$  depends on the ratio of the thermal resistances ( $R_{\text{in}}/R_{\text{ex}}$ ) from Eq. (3). Furthermore, both  $a$  and  $\gamma_{\text{th}}$  are independent of  $T_e$ . The term  $2/\gamma_{\text{th}}$  represents the characteristic length of the heat dissipation, indicating that the heating effect decreases by  $1/e$ . Thereby, the temperature independent parameters  $a$  and  $\gamma_{\text{th}}$  thermally characterize the QD array structure.

Here, we extend our model to the case of multiple heat sources. Typically, the electron temperature is written as  $T_e' = \sqrt{T_{\text{MXC}}^2 + T_e^2}$ , where  $T_e'$ ,  $T_{\text{MXC}}$ , and  $T_e$  are the measurable temperature, the base temperature of refrigerator, and electron temperature, respectively<sup>15,34</sup>. Consistent with this notation, we employ the following model, i.e., the total rise in electron temperature  $T_e^{\text{total}}$  due to multiple heat sources is calculated using the root sum square as

$$T_e^{\text{total}} = \sqrt{\sum_{i=1}^N (\Delta T_e^i)^2}, \quad (6)$$

where  $N$  is the number of heat sources and  $\Delta T_e^i$  is the rise in electron temperature due to the  $i$ -th heat source. From Eq. (6), Eq. (5) can be rewritten under the background temperature  $T_0$  as

$$T_e^{\text{total}} = \sqrt{T_e^2 + T_0^2} = ae^{-\frac{\gamma_{\text{th}}}{2}D}\sqrt{P + P_0}, \quad (7)$$

where  $T_0 = ae^{-\frac{\gamma_{\text{th}}}{2}D}\sqrt{P_0}$ , and  $P_0$  is the background heating power. We use this equation to fit experimental results. Note that in our experiment,  $T_0$  and  $P_0$  includes the effect of lifetime broadening and charge noise broadening<sup>34</sup>.

### III. EXPERIMENT

#### A. Device structure

To verify the proposed thermal model, we experimentally measure  $T_e$  in a QD array. Figure 3(a) shows the device structure<sup>37</sup>. In this device, we can measure the temperature at different distances from the heating point. The T-shaped silicon channel (green) is fabricated using silicon on insulator (SOI), and multiple polysilicon gate electrodes are formed on the T-shaped Si channel. The horizontal channel is covered with first gates (BG0-BG3, light blue) and second gates (PG0-PG3, blue), for a total of seven gates. These fine-pitch gate structures are fabricated using the self-align patterning process<sup>8,38</sup>. Each gate has terminals on both sides, allowing current to flow through them by applying DC voltages through wiring connected to instruments at room temperature.

Another second gate (SGS, red) and other third gates (TG1 and TG2, orange) on the vertical channel comprise a single-electron transistor (SET), and temperature around the SET can be measured using CBT as described below. In this experiment, we treat the temperature measured by the SET as the electron temperature  $T_e$ .

The four first gates (BG0-BG3) are used as heat sources by flowing current through each gate. Figure 3(b) shows the cross-section between A and A' in Fig. 3(a). Corresponding to the model shown in Fig. 2(a), the unit cell length of this device is  $L_{\text{cell}} = 120$  nm (we also measure the device of  $L_{\text{cell}} = 160$  nm, see Appendix B).

The silicon chip with the above structure is glued to a cryogenic printed circuit board (QBoard, Qdevil) using silver paste, and each terminal is wired using aluminum bonding wire. Measurements were performed using a dilution refrigerator (Proteox, Oxford Instruments) with a base temperature of 8 mK.

#### B. Measurement

We use CBT to estimate the local temperature at the SET. In CBT, there are several restrictions for QD parameters for accurately measuring temperature, e.g., the tunnel rate of barriers of SET  $h\Gamma$ , energy spacing of the quantum levels  $\Delta E$ , thermal energy  $k_B T$ , and charging energy  $e^2/C$ <sup>26</sup>. In this experiment, we use the classical regime, i.e.,  $h\Gamma \ll \Delta E \ll k_B T \ll e^2/C$ . By measuring the current  $I_d$  flowing through the SET while sweeping the voltage of the SGS gate  $V_g$  and the drain  $V_d$  [Fig. 4(a)], we can obtain the SGS gate voltage dependence of the differential conductance  $G = dI_d/dV_d$  [Fig. 4(b)] and estimate the electron temperature around SET  $T_e$ . The differential conductance  $G$  in the region where  $V_d$  is small is<sup>26</sup>

$$\frac{G}{G_{\text{max}}} = \frac{\alpha e (V_g - V_0)}{k_B T_e \sinh\left(\frac{\alpha e (V_g - V_0)}{k_B T_e}\right)} \approx \cosh^{-2}\left(\frac{\alpha e (V_g - V_0)}{2.5 k_B T_e}\right), \quad (8)$$

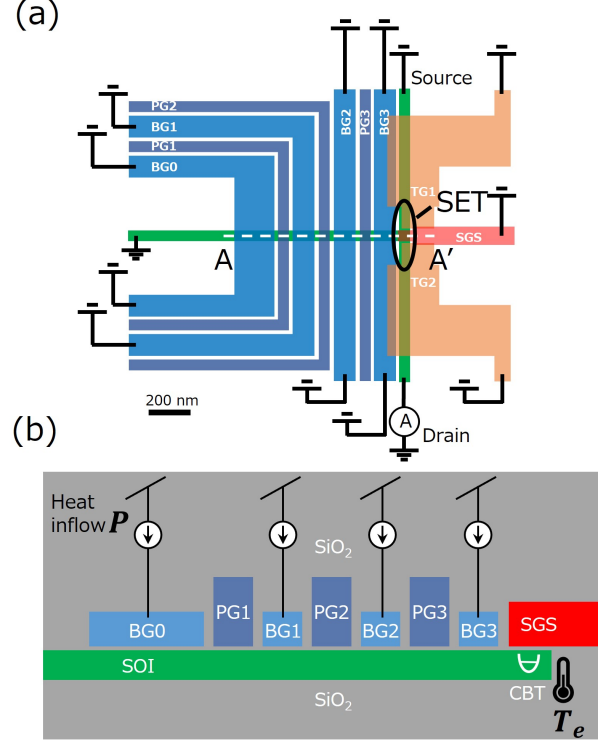


FIG. 3. (a) Schematic diagram of the device structure and setup for electron temperature measurement. An SOI channel (green), BGs (light blue), TGs (orange), and SGS (red) have electrodes to apply voltages, where each wiring is a twisted cable made of phosphor bronze and has a low pass filter mounted on Qboard. (b) Schematic diagram of the cross-section at A-A' in (a). The BGs made of polysilicon are used as a heater by flowing current. Gate SGS is used as the plunger gate in SET.

where  $G_{\text{max}}$ ,  $\alpha$ ,  $e$ ,  $k_B$ , and  $V_0$  are the peak value of  $G$ , the lever arm, the elementary charge, the Boltzmann constant, and the voltage value at  $G_{\text{max}}$ , respectively. The lever arm was estimated as  $\alpha = 0.08$  by obtaining the Coulomb diamond shown in Fig. 4(a). Figure 4(c) and 4(d) show examples of  $G$  (Coulomb peak) at different  $T_e$  situations. It can be confirmed that the Coulomb peak shape reflects the change in  $T_e$ , and  $T_e$  can be estimated by fitting the experimental result by the curve of Eq. (8). This measurement method is constrained by the tunnel rate and can be used in the range  $k_B T_e \gg h\Gamma$ , where  $h\Gamma/k_B \sim 1$  K in this experiment.

We use a local heater by applying a current to each of the four gate electrodes BG0-BG3 as shown in Fig. 5(a). If the electric field around the SET changes during the measurement, the SET conditions are affected by the electric field and the temperature measurement cannot be performed correctly. Therefore, we apply a voltage of  $+V/2$  and  $-V/2$ , where  $V = \sqrt{RP}$  ( $R$  is the resistance of the entire gate wiring) to each terminal of the gate to allow current to flow through the gate. Due to the symmetry of the wiring structure in the dilution refrigerator,

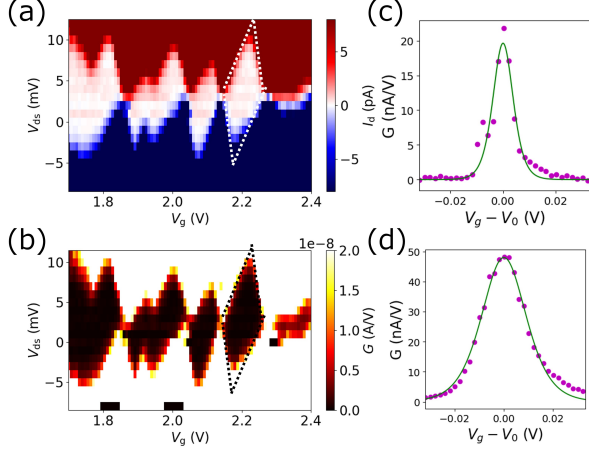


FIG. 4. (a,b) Coulomb diamond of (a) the drain current of SET  $I_d$  and (b) the differential conductance of SET  $G$ . The (a) white and (b) black dotted lines show one of the Coulomb diamond areas. (c) and (d) show examples of Coulomb peak and fitting curve with Eq. (8) at different temperatures. The estimated temperatures are (c) 2.4 K and (d) 5.5 K.

we set the voltage to be approximately zero on the channel. This stabilizes the SET condition because the voltage condition around the SET is stable even if the heating power  $P$  is changed by varying  $V$ , where  $P = V^2/R$ . We measure the resistance of each gate wiring excluding the additional resistance on the circuit board for a low pass filter and use these values to calculate  $P$ , considering that the polysilicon gate has the dominant resistance among all of the gate wiring.

Figure 5(b) shows the experimental results of  $T_e$  as a function of the heating power  $P$  when each gate is used as a heat source. As expected,  $T_e$  increases monotonically with  $P$  and  $1/D$ . The experimental results can be fitted using Eq. (7) as

$$T_e = A_i \sqrt{P + P_0}, \quad (9)$$

where ( $i \in \{\text{BG0, BG1, BG2, BG3}\}$ ) [see the dotted curves in Fig. 5(b)]. The best-fit results are  $A_{\text{BG0}} = 2.2 \text{ K}/\sqrt{\mu\text{W}}$ ,  $A_{\text{BG1}} = 4.0 \text{ K}/\sqrt{\mu\text{W}}$ ,  $A_{\text{BG2}} = 5.5 \text{ K}/\sqrt{\mu\text{W}}$ ,  $A_{\text{BG3}} = 8.5 \text{ K}/\sqrt{\mu\text{W}}$ , where  $A_i$  depends on the distance  $D$  between the measurement point and the heat source. The inset of Fig. 5(b) plots  $A_i$  and shows the best-fit curve with  $A = ae^{-\frac{\gamma_{\text{th}}}{2}D}$  from Eq. (5), where the device-dependent parameters are  $a = 8.5 \text{ K}/\sqrt{\mu\text{W}}$  and  $2/\gamma_{\text{th}} = 280 \text{ nm}$ . We experimentally confirm that  $T_e$  rises is proportional to  $\sqrt{P}$  as in the model, and the heating effect of distance is reduced exponentially as expected.

We measure another device of different gate pitch as shown in Appendix B. From these results, we conclude that the proposed model successfully reproduces the experimental results. This demonstrates its capability to model the thermal conduction characteristics of silicon QD array structures effectively.

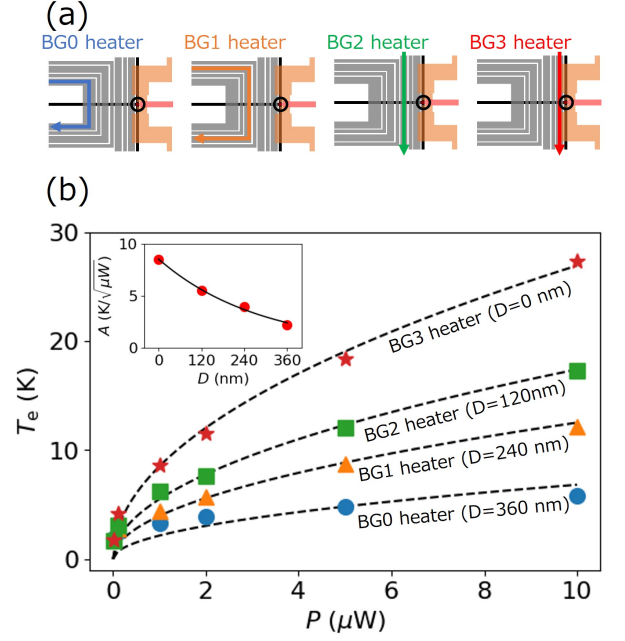


FIG. 5. (a) Schematic of local heaters by flowing current in barrier gates. The resistance of each gate excluding the resistance of the low pass filter in Qboard at cryogenic temperatures are  $R_{\text{BG0}} = 78.8 \text{ k}\Omega$ ,  $R_{\text{BG1}} = 78.1 \text{ k}\Omega$ ,  $R_{\text{BG2}} = 70.9 \text{ k}\Omega$  and  $R_{\text{BG3}} = 61.3 \text{ k}\Omega$ , respectively. (b) Experimental results of  $T_e$  as a function of  $P$  and  $D$ . The dotted curves are the best-fit results with Eq. (9). The inset shows the best-fit results of  $A$  as a function of  $D$  and the dotted curve is the best-fit result with  $A = ae^{-\frac{\gamma_{\text{th}}}{2}D}$ , where  $a = 8.5 \text{ K}/\sqrt{\mu\text{W}}$  and  $2/\gamma_{\text{th}} = 280 \text{ nm}$ .

#### IV. DISCUSSION

To consider the limitations of our model, we re-summarize the assumptions for deriving Eq. (4) according to the above discussions: (i) The thermal circuit of the model is an infinite periodic structure, (ii)  $R_{\text{in}}$  and  $R_{\text{ex}}$  are temperature dependent and spatially uniform, and (iii) the net effective temperature of the QD array is proportional to  $T_e$ . Moreover, for deriving Eq. (5), we also assume that the temperature dependence of  $R_{\text{in}}$  and  $R_{\text{ex}}$  are metallic ( $\beta_{\text{in}} \approx \beta_{\text{ex}} \approx 1$ ). Despite these potential sources of modeling error, the consistency between the experimental results and the model supports the validity of our simplifications. The model validity is further investigated using the order estimation in Appendix C.

We also discuss how to design the QD array structure. To mitigate the thermal effects on the qubits, based on Eq. (5), the following conditions should be met: (I)  $P$  should be reduced, (II)  $D$  should be increased, and (III) the device-dependent parameters  $a$  and  $2/\gamma_{\text{th}}$  should be minimized. Conditions (I) and (II) are straightforward, i.e., the amount of heating power needs to be reduced, for example, by lowering the electrical resistance of the gate, and the qubits need to be kept appropriately dis-

tant from the heat sources. Our main result is condition (III), which is useful for quantitative thermal design of the QD array structures. Reducing  $a$  implies that even if the heating power is high, the temperature rise is low; in other words, the structure does not easily accumulate heat. To reduce  $a \propto \sqrt[4]{R_{\text{in}}R_{\text{ex}}}$ , the thermal resistance of the entire structure should be minimized. On the other hand, reducing  $2/\gamma_{\text{th}}$  (the characteristic length) means creating a structure that makes it difficult to transport heat to the qubits. To reduce  $2/\gamma_{\text{th}} \approx 2\sqrt{R_{\text{ex}}/R_{\text{in}}}$ , the ratio of heat dissipation to heat inflow should be increased. For example, an additional metallic heat sink at the top and bottom of the gate layer can be effective. This can be achieved using technologies such as through-silicon vias (TSVs)<sup>39</sup>.

The next challenge is to find a way to simultaneously achieve both high QD (or qubit) performance and thermal tolerance. To further comprehensively optimize the QD array structure, the effect of  $T_e$  on the fidelity of quantum computing needs to be quantitatively estimated. The rise in  $T_e$  is known to lead to shorter coherence times, degraded readout fidelity, and increased charge noise (low operation fidelity)<sup>2,10</sup>. However, these quantitative evaluations have yet to be clarified, except for certain readout fidelity<sup>40</sup>, suggesting that further experimental and theoretical studies are necessary.

In future work, we will investigate the thermal dynamic model of the QD array structure to control the heat sources using real-time ambient temperature measurements. The thermal dynamic model is also strongly related to the operation fidelity of qubits, including the heat-induced frequency shift<sup>14,16,36</sup>. This will be modeled by the heat capacitance  $C_{\text{ex}}$  and measured by a high-speed readout method such as reflectometry<sup>35</sup>.

In conclusion, we proposed a simple thermal circuit model for the silicon QD array structure and validated our model in experiments. Our proposed model is intuitive, simple, and scalable and is applicable to the wide spread of the QD array structures for thermal analysis.

## ACKNOWLEDGMENTS

We acknowledge N. Mertig and A. Ramsay at Hitachi Cambridge Laboratory for helpful discussions. This work is supported by JST Mooshot R&D Grant No. JP-MJMS2065.

### Appendix A: Thermophysical properties

We summarize thermophysical properties of represented materials in the typical silicon fabrication process based on Refs.<sup>41–43</sup>, as shown in Fig. 6.

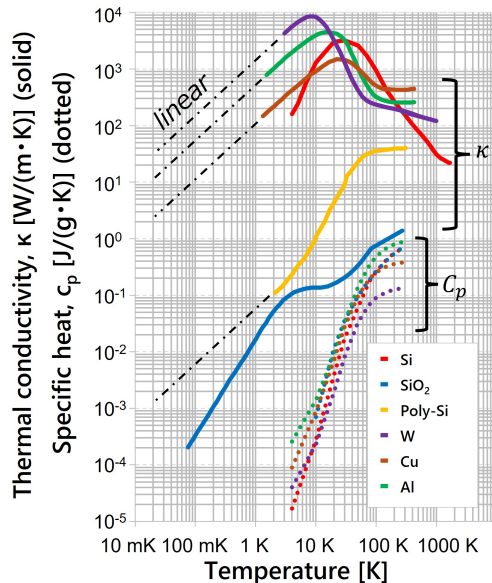


FIG. 6. Thermophysical properties of represented materials where  $\kappa$  of metallic materials (W, Cu, Al, and Poly-Si) are extrapolated by linear function ( $\propto T$ ) in the cryo-temperature regime<sup>41,42</sup>. Note that Si is single crystal<sup>43</sup>, SiO<sub>2</sub> is amorphous<sup>42</sup>, and Poly-Si is P-type polysilicon (B-doped =  $3 \times 10^{20}$  atom/cm<sup>3</sup>)<sup>43</sup>.

### Appendix B: Measurement result of device B

We measure another device with  $L_{\text{cell}} = 160$  nm (device B), similar to the device described in the main text (device A). Figure 7 shows the results, which exhibit the same trend as those in Fig. 5. However, the electron temperature is lower than that of device A. This is attributed to the larger gate pitch, which implies a longer gate length and a higher ratio of the polysilicon gate to the insulator. This configuration likely decreases the resistance  $R_{\text{in}}$  while maintaining  $R_{\text{ex}}$ , resulting in an increased thermal characteristic length  $2/\gamma_{\text{th}} \approx 2\sqrt{R_{\text{ex}}/R_{\text{in}}}$ . On the other hand,  $a \propto \sqrt[4]{R_{\text{in}}R_{\text{ex}}}$  changes minimally due to the fourth root. This measurement further validates the proposed thermal model. In Appendix C, we further summarize the experimental results.

### Appendix C: Summary of experimental results and order estimation of heat inflow resistance

Table I presents the device-dependent parameters estimated from the experiments, where we compare devices A (main text) and B (Appendix B). To evaluate the thermal resistances, we use the relations of  $R_{\text{in}}T_e = a^2\gamma_{\text{th}}$  and  $R_{\text{ex}}T_e = a^2/\gamma_{\text{th}}$  derived from Eqs. (2) and (3), where  $\beta = 1$  is used. We analyze these results to the order estimation values of heat inflow resistance  $R_{\text{in}}^{\text{est}}$  on the basis of the device structures and the thermophysical prop-

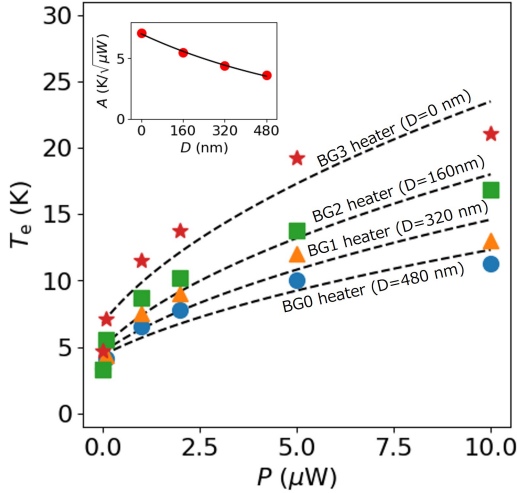


FIG. 7. Experimental results of  $T_e$  as a function of  $P$  and  $D$  in device B of  $L_{\text{cell}} = 160$  nm. The dotted curves are the best-fit results with Eq. (9). The inset shows the best-fit results of  $A$  as a function of  $D$  and the dotted curve is the best-fit result with  $A = ae^{-\frac{3}{2}D/700}$ , where  $a = 7.0$  K/ $\sqrt{\mu\text{W}}$  and  $2/\gamma_{\text{th}} = 700$  nm.

	Device A	Device B
$L_{\text{cell}}$ (nm)	120	160
$a$ (K/ $\sqrt{\mu\text{W}}$ )	8.5	7.0
$2/\gamma_{\text{th}}$ (nm)	280	700
$R_{\text{in}}T_e$ ( $\text{K}^2/(\text{m}\cdot\text{W})$ )	$5.1 \times 10^{14}$	$1.4 \times 10^{14}$
$R_{\text{ex}}T_e$ ( $\text{K}^2\cdot\text{m}/\text{W}$ )	10	17
$R_{\text{in}}^{\text{est}}$ ( $\text{K}^2/(\text{m}\cdot\text{W})$ )	$4.0 \times 10^{14}$	$3.5 \times 10^{14}$

TABLE I. The device-dependent parameters calculated from the experimental results, and order estimation results (the last row).

erties shown in Fig. 6 (see Appendix B). Note that the order estimation of  $R_{\text{ex}}$  is difficult due to the complicated heat dissipation path.

Using the model of the QD array structure shown in Fig. 2 analogous to the series resistance, we estimate  $R_{\text{in}}^{\text{est}}$  as

$$R_{\text{in}}^{\text{est}} = \frac{1}{SL_{\text{cell}}} \left( \frac{L_{\text{PolySi}}}{\kappa_{\text{PolySi}}} + \frac{L_{\text{SiO}_2}}{\kappa_{\text{SiO}_2}} \right), \quad (\text{C1})$$

where  $S$  is the cross-sectional area of the heat inflow path,  $L_{\text{PolySi}}$  ( $L_{\text{SiO}_2}$ ) is the total length of the polysilicon gates BG and PG ( $\text{SiO}_2$ ), where  $L_{\text{cell}} = L_{\text{PolySi}} + L_{\text{SiO}_2}$ , and  $\kappa_{\text{PolySi}}$  ( $\kappa_{\text{SiO}_2}$ ) is the thermal conductivity of the polysilicon gates ( $\text{SiO}_2$ ). We use  $S = 10^{-13}$  m<sup>2</sup>, where  $S$  is calculated as the product of the width ( $W$ ) and height ( $H$ ) of the heat inflow path and we use  $W = 1$   $\mu\text{m}$  and  $H = 0.1$   $\mu\text{m}$ . From the device structure, we use  $L_{\text{PolySi}} = 90$  nm for device A and  $L_{\text{PolySi}} = 130$  nm for device B, while  $L_{\text{SiO}_2} = 30$  nm for both devices. From the thermophysical properties shown in Fig. 6, we use

$\kappa_{\text{PolySi}} = 0.05$  W/(m $\cdot$ K) and  $\kappa_{\text{SiO}_2} = 0.01$  W/(m $\cdot$ K) assuming around 1 K. We obtain the estimation results as  $R_{\text{in}}^{\text{est}} = 4.0 \times 10^{14}$  for device A and  $R_{\text{in}}^{\text{est}} = 3.5 \times 10^{14}$  for device B at  $T_e = 1$  K, as shown in Table I. The lower  $R_{\text{in}}$  for device B than for device A is consistent with the experimental trend. This result demonstrates the validity of our model. Additionally, the order of  $R_{\text{in}}^{\text{est}}$  values are comparable to the experimental results at  $T_e = 1$  K, validating the formulation in Eq. C1 at least for the order estimation. We also expect that by improving this simple model or combining it with different approaches, e.g., finite element simulations, we can develop a framework for predicting thermal characteristics more reliably and accurately.

- <sup>1</sup>G. Burkard, T. D. Ladd, A. Pan, J. M. Nichol, and J. R. Petta, "Semiconductor spin qubits," *Reviews of Modern Physics* **95**, 025003 (2023).
- <sup>2</sup>T. Kodera, "Trends and prospects for semiconductor qubit research," *JSAF Review* **2024**, 240101 (2024).
- <sup>3</sup>L. M. K. Vandersypen, H. Bluhm, J. S. Clarke, A. S. Dzurak, R. Ishihara, A. Morello, D. J. Reilly, L. R. Schreiber, and M. Veldhorst, "Interfacing spin qubits in quantum dots and donors -hot, dense, and coherent," *NPJ Quantum Inf.* **3**, 34 (2017).
- <sup>4</sup>M. Veldhorst, H. G. J. Eenink, C.-H. Yang, and A. S. Dzurak, "Silicon cmos architecture for a spin-based quantum computer," *Nature communications* **8**, 1766 (2017).
- <sup>5</sup>F. Borsoi, N. W. Hendrickx, V. John, M. Meyer, S. Motz, F. van Riggelen, A. Sammak, S. L. de Snoo, G. Scappucci, and M. Veldhorst, "Shared control of a 16 semiconductor quantum dot crossbar array," *Nature Nanotechnology* **19**, 21–27 (2024).
- <sup>6</sup>R. Li, L. Petit, D. P. Franke, J. P. Dehollain, J. Helsen, M. Steudtner, N. K. Thomas, Z. R. Yoscovits, K. J. Singh, S. Wehner, *et al.*, "A crossbar network for silicon quantum dot qubits," *Science advances* **4**, eaar3960 (2018).
- <sup>7</sup>S. G. J. Philips, M. T. Madzik, S. V. Amitonov, S. L. D. Snoo, M. Russ, N. Kalhor, C. Volk, W. I. L. Lawrie, D. Brousse, L. Trypuzen, *et al.*, "Universal control of a six-qubit quantum processor in silicon," *Nature* **609**, 919–924 (2022).
- <sup>8</sup>N. Lee, R. Tsuchiya, G. Shinkai, Y. Kanno, T. Mine, T. Takahama, R. Mizokuchi, T. Kodera, D. Hisamoto, and H. Mizuno, "Enhancing electrostatic coupling in silicon quantum dot array by dual gate oxide thickness for large-scale integration," *Appl. Phys. Lett.* **116**, 162106 (2020).
- <sup>9</sup>N. Lee, R. Tsuchiya, Y. Kanno, T. Mine, Y. Sasago, G. Shinkai, R. Mizokuchi, J. Yoneda, T. Kodera, C. Yoshimura, S. Saito, D. Hisamoto, and H. Mizuno, "16 x 8 quantum dot array operation at cryogenic temperatures," *Jpn. J. Appl. Phys.* **61**, 1040 (2022).
- <sup>10</sup>J. Y. Huang, R. Y. Su, W. H. Lim, M. Feng, B. van Straaten, B. Severin, W. Gilbert, N. Dumoulin Stuyck, T. Tantt, S. Serano, *et al.*, "High-fidelity spin qubit operation and algorithmic initialization above 1 k," *Nature* **627**, 772–777 (2024).
- <sup>11</sup>S. Krinmer, S. Storz, P. Kurpiers, P. Magnard, J. Heinsoo, R. Keller, J. Lütolf, C. Eichler, and A. Wallraff, "Engineering cryogenic setups for 100-qubit scale superconducting circuit systems," *EPJ Quantum Technol.* **6**, 2 (2019).
- <sup>12</sup>A. M. Savin, J. P. Pekola, D. V. Averin, and V. K. Semenov, "Thermal budget of superconducting digital circuits at subkelvin temperatures," *Journal of applied physics* **99** (2006).
- <sup>13</sup>E. Kawakami, P. Scarlino, L. R. Schreiber, J. R. Prance, D. E. Savage, M. G. Lagally, M. A. Eriksson, and L. M. K. Vandersypen, "Excitation of a si/sige quantum dot using an on-chip microwave antenna," *Applied Physics Letters* **103** (2013).
- <sup>14</sup>K. Takeda, J. Yoneda, T. Otsuka, T. Nakajima, M. Delbecq, G. Allison, Y. Hoshi, N. Usami, K. Itoh, S. Oda, *et al.*, "Optimized electrical control of a si/sige spin qubit in the presence

- of an induced frequency shift,” *npj Quantum Information* **4**, 54 (2018).
- <sup>15</sup>G. M. Noah, T. H. Swift, M. De Kruijf, A. Gomez-Saiz, J. J. Morton, and M. F. Gonzalez-Zalba, “Cmos on-chip thermometry at deep cryogenic temperatures,” *Applied Physics Reviews* **11** (2024).
- <sup>16</sup>B. Undseth, O. Pietx-Casas, E. Raymenants, M. Mehmandoust, M. T. Mkdzik, S. G. Philips, S. L. De Snoo, D. J. Michalak, S. V. Amitonov, L. Tryputen, *et al.*, “Hotter is easier unexpected temperature dependence of spin qubit frequencies,” *Physical Review X* **13**, 041015 (2023).
- <sup>17</sup>X. Xue, B. Patra, J. P. G. V. Dijk, N. Samkharadze, S. Subramanian, A. Corna, B. P. Wuetz, C. Jeon, F. Sheikh, E. Juarez-Hernandez, *et al.*, “Cmos-based cryogenic control of silicon quantum circuits,” *Nature* **593**, 205–210 (2021).
- <sup>18</sup>S. Pauka, K. Das, R. Kalra, A. Moini, Y. Yang, M. Trainer, A. Bousquet, C. Cantaloube, N. Dick, G. Gardner, *et al.*, “A cryogenic cmos chip for generating control signals for multiple qubits,” *Nature Electronics* **4**, 64–70 (2021).
- <sup>19</sup>S. K. Bartee, W. Gilbert, K. Zuo, K. Das, T. Tanttu, C. H. Yang, N. D. Stuyck, S. J. Pauka, R. Y. Su, W. H. Lim, *et al.*, “Spin qubits with scalable milli-kelvin cmos control,” arXiv preprint arXiv:2407.15151 (2024).
- <sup>20</sup>L. Petit, J. M. Boter, H. G. J. Eenink, G. Droulers, M. L. V. Tagliaferri, R. Li, D. P. Franke, K. J. Singh, J. S. Clarke, R. N. Schouten, V. V. Dobrovitski, L. M. K. Vandersypen, and M. Veldhorst, “Spin lifetime and charge noise in hot silicon quantum dot qubits,” *Phys. Rev. Lett.* **121**, 076801 (2018).
- <sup>21</sup>K. Ono, T. Mori, and S. Moriyama, “High-temperature operation of a silicon qubit,” *Scientific reports* **9**, 469 (2019).
- <sup>22</sup>L. Petit, H. G. J. Eenink, M. Russ, W. I. L. Lawrie, N. W. Hendrickx, S. G. J. Philips, J. S. Clarke, L. M. K. Vandersypen, and M. Veldhorst, “Universal quantum logic in hot silicon qubits,” *Nature* **580**, 355–359 (2020).
- <sup>23</sup>C. H. Yang, R. C. C. Leon, J. C. C. Hwang, A. Saraiva, T. Tanttu, W. Huang, J. C. Lemyre, K. W. Chan, K. Y. Tan, F. E. Hudson, *et al.*, “Operation of a silicon quantum processor unit cell above one kelvin,” *Nature* **580**, 350–354 (2020).
- <sup>24</sup>L. Petit, M. Russ, G. H. G. J. Eenink, W. I. L. Lawrie, J. S. Clarke, L. M. K. Vandersypen, and M. Veldhorst, “Design and integration of single-qubit rotations and two-qubit gates in silicon above one kelvin,” *Communications Materials* **3**, 82 (2022).
- <sup>25</sup>L. C. Camenzind, S. Geyer, A. Fuhrer, R. J. Warburton, D. M. Zumbühl, and A. V. Kuhlmann, “A hole spin qubit in a fin field-effect transistor above 4 kelvin,” *Nature Electronics* **5**, 178–183 (2022).
- <sup>26</sup>C. W. J. Beenakker, “Theory of coulomb-blockade oscillations in the conductance of a quantum dot,” *Phys. Rev. B* **44**, 1646–1656 (1991).
- <sup>27</sup>F. Giazotto, T. T. Heikkilä, A. Luukanen, A. M. Savin, and J. P. Pekola, “Opportunities for mesoscopics in thermometry and refrigeration: Physics and applications,” *Reviews of Modern Physics* **78**, 217 (2006).
- <sup>28</sup>A. Rossi, T. Ferrus, and D. Williams, “Electron temperature in electrically isolated si double quantum dots,” *Applied Physics Letters* **100** (2012).
- <sup>29</sup>L. W. Molenkamp, T. Gravier, H. van Houten, O. J. A. Buijk, M. A. A. Mabesoone, and C. T. Foxon, “Peltier coefficient and thermal conductance of a quantum point contact,” *Phys. Rev. Lett.* **68**, 3765–3768 (1992).
- <sup>30</sup>O. Chiatti, J. T. Nicholls, Y. Y. Proskuryakov, N. Lumpkin, I. Farrer, and D. A. Ritchie, “Quantum thermal conductance of electrons in a one-dimensional wire,” *Phys. Rev. Lett.* **97**, 056601 (2006).
- <sup>31</sup>E. A. Hoffmann, N. Nakpathomkun, A. I. Persson, H. Linke, H. A. Nilsson, and L. Samuelson, “Quantum-dot thermometry,” *Applied Physics Letters* **91** (2007).
- <sup>32</sup>E. A. Hoffmann, H. A. Nilsson, J. E. Matthews, N. Nakpathomkun, A. I. Persson, L. Samuelson, and H. Linke, “Measuring temperature gradients over nanometer length scales,” *Nano Letters* **9**, 779–783 (2009).
- <sup>33</sup>B. Dutta, J. T. Peltonen, D. S. Antonenko, M. Meschke, M. A. Skvortsov, B. Kubala, J. König, C. B. Winkelmann, H. Courtois, and J. P. Pekola, “Thermal conductance of a single-electron transistor,” *Phys. Rev. Lett.* **119**, 077701 (2017).
- <sup>34</sup>M. de Kruijf, G. M. Noah, A. Gomez-Saiz, J. J. Morton, and M. F. Gonzalez-Zalba, “Measurement of cryoelectronics heating using a local quantum dot thermometer in silicon,” *Chip*, 100097 (2024).
- <sup>35</sup>V. Champain, V. Schmitt, B. Bertrand, H. Niebojewski, R. Maurand, X. Jehl, C. Winkelmann, S. De Franceschi, and B. Brun, “Real-time millikelvin thermometry in a semiconductor-qubit architecture,” *Phys. Rev. Appl.* **21**, 064039 (2024).
- <sup>36</sup>Y. Sato and T. Kawahara, “Simulation of temperature-dependent quantum gates in silicon quantum dots with frequency shifts,” arXiv preprint arXiv:2407.05295 (2024).
- <sup>37</sup>T. Utsugi, N. Lee, R. Tsuchiya, T. Mine, R. Mizokuchi, J. Yoneda, T. Kodera, S. Saito, D. Hisamoto, and H. Mizuno, “Single-electron pump in a quantum dot array for silicon quantum computers,” *Japanese Journal of Applied Physics* **62**, SC1020 (2023).
- <sup>38</sup>“To be published.” .
- <sup>39</sup>M. Taguchi, T. Okidono, T. Miki, and M. Nagata, “Si interposer with cu tsvs on cu substrate thermally and electrically anchoring qubit chips in millikelvin assembly,” in *2024 IEEE 74th Electronic Components and Technology Conference (ECTC)* (IEEE, 2024) pp. 447–450.
- <sup>40</sup>D. Keith, S. Gorman, L. Kranz, Y. He, J. Keizer, M. Broome, and M. Simmons, “Benchmarking high fidelity single-shot readout of semiconductor qubits,” *New Journal of Physics* **21**, 063011 (2019).
- <sup>41</sup>P. Duthil, “Material properties at low temperature,” CAS - CERN Accelerator School, 77–95 (2014).
- <sup>42</sup>J. Ekin, *Experimental techniques for low-temperature measurements: cryostat design, material properties and superconductor critical-current testing* (Oxford university press, 2006).
- <sup>43</sup>*Thermophysical Property Database*, National Institute of Advanced Industrial Science and Technology.